Magnetic component of narrowband ion cyclotron waves in the auroral zone

O. Santolík,[1] J. S. Pickett, and D. A. Gurnett
Department of Physics and Astronomy, University of Iowa, Iowa City, Iowa, USA

L. R. O. Storey
Quartier Luchène, Cucuron, France

Received 23 May 2001; revised 9 July 2002; accepted 10 July 2002; published 17 December 2002.

[1] We report observations of waves near the local proton cyclotron frequency and its lowest harmonics, made by the Plasma Wave Instrument on board the Polar spacecraft, on orbits for which the perigee (at an altitude of 1 Earth radius) was in or near the southern auroral zone. The electromagnetic nature of these waves was revealed by measuring their magnetic components simultaneously with two independent antenna systems, one a single loop and the other a set of triaxial search coils. Waves of this kind were found in the southern auroral zone on about a third of the orbits examined. Peaks in the magnetic field power spectra occurred at frequencies both below and above the fundamental cyclotron frequency. The ratio of the amplitudes of the electric and magnetic fluctuations was usually greater than the speed of light, suggesting that we observe a magnetic component related to the wave mode customarily called electrostatic ion cyclotron waves. The fluctuating vector of the wave magnetic field was in or close to the plane perpendicular to the static magnetic field. Our main result is that its polarization, which covered a broad range from left-hand elliptic to right-hand elliptic, can be explained by the superposition of many linearly polarized waves. *INDEX TERMS:* 2772 Magnetospheric Physics: Plasma waves and instabilities; 2704 Magnetospheric Physics: Auroral phenomena (2407); 6984 Radio Science: Waves in plasma; 7871 Space Plasma Physics: Waves and instabilities; *KEYWORDS:* Auroral zone, ion cyclotron waves, polarization analysis

Citation: Santolík, O., J. S. Pickett, D. A. Gurnett, and L. R. O. Storey, Magnetic component of narrowband ion cyclotron waves in the auroral zone, *J. Geophys. Res.*, *107*(A12), 1444, doi:10.1029/2001JA000146, 2002.

1. Introduction

[2] Waves near the fundamental and the lowest harmonics of the proton cyclotron frequency have been reported from spacecraft observations on S3-3 [*Kintner et al.*, 1978, 1979], ISIS 2 [*Yoshino*, 1991], Viking [*André et al.*, 1987], and ISEE [*Cattell et al.*, 1991]. They occurred on auroral field lines in a wide range of altitudes from below 0.5 R_E (Earth radii) up to more than 3 R_E. The main feature of the wave spectra is the principal peak near the local proton cyclotron frequency; it is often accompanied by peaks at a few (typically one or two) higher harmonics. These waves have often been labeled as electrostatic, though direct measurements showing the wave magnetic field to be negligible were not often made. *Kinter* [1980] described two distinct types of ion cyclotron phenomena, electrostatic ion cyclotron (EIC) waves and ion cyclotron harmonic (ICH) waves, the former corresponding to the observations near the first few cyclotron frequency harmonics, whereas the latter extended to higher harmonics. In some related theoretical work, *André* [1985] studied wave modes in a Maxwellian plasma with a low ion temperature (2 eV) and found both EIC and ICH waves as banded electrostatic ion Bernstein or Bernstein-like modes. For waves with a nonzero component of the wave vector in the direction parallel to the static magnetic field ($\boldsymbol{B}_0$), the generation was attributed to unstable distributions of the parallel component of particle velocity, due either to upgoing ion beams [e.g., *André et al.*, 1987] or to parallel currents carried by drifting electrons [e.g., *Bergmann*, 1984; *Cattell et al.*, 1991, 1998]. Saturation of linearly excited EIC parent waves by coherent decay to the observed daughter EIC and ion acoustic modes was also considered [*Bergmann and Hudson*, 1987]. Near Io, similar emissions at the cyclotron frequencies of heavy ions were explained by the interaction of waves with a perpendicular ring distribution of pickup ions [*Russell and Kivelson*, 2000], and wave-particle interactions with ring distributions of H^+ and He^{++} ions have also been studied in the Earth's cusp regions [e.g., *Roth and Hudson*, 1985].

[3] *Mozer et al.* [1997] reported very large amplitudes (up to 1.5 V/m) for nonlinear electric field fluctuations measured by the electric field experiment on the Polar spacecraft;

[1]Now at Faculty of Mathematics and Physics, Charles University, Prague, and at Institute of Atmospheric Physics, Czech Academy of Sciences, Prague, Czech Republic.

0148-0227/02/2001JA000146$09.00

their period was close to that of proton cyclotron motion. Accompanying magnetic field fluctuations with the same period and with an amplitude of 0.2 nT were also observed, but their polarization was not examined. *Chaston et al.* [1998] recently analyzed a case where the FAST spacecraft observed peaks near harmonics of the proton cyclotron frequency in the magnetic field data. These waves were observed on auroral field lines at an altitude of 0.65 R_E, and their magnetic field oscillated in the plane perpendicular to $\boldsymbol{B}_0$. The authors reported both left- and right-hand polarization with ellipticity often below 0.5 and predominantly upward propagation. The ratio of the amplitudes of the electric and magnetic fluctuations was close to the speed of light (c), which means that the magnetic components were more intense, in relation to the electric components, than those for the waves observed by *Mozer et al.* [1997].

[4] The aim of the present paper is to describe measurements of magnetic fluctuations near the fundamental and the lowest harmonics of the proton cyclotron frequency, made by the Plasma Wave Instrument (PWI) on the Polar spacecraft [*Gurnett et al.*, 1995], and to investigate their polarization and coherence. The waves have spectra like those of the EIC waves of *Kintner* [1980]. The results of our analysis, which are consistent with those of *Chaston et al.* [1998], suggest that we indeed observe a magnetic component of the so-called EIC waves. Moreover, we show that the observations can be explained by the superposition of many linearly polarized waves. In sections 2 and 3 we present our data set and analysis methods, and we show in some detail unique measurements made simultaneously by two independent magnetic antenna systems, the loop and the triaxial search coils. In section 4 we describe further observations of these waves, in a comprehensive study of several tens of cases. In section 5 we examine their coherence and polarization by means of numerical simulations. Finally, in section 6 we discuss the implications of these results, and we draw some conclusions.

2. Observations

[5] Figure 1 shows a time-frequency spectrogram of data recorded on 5 June 1996 by the wideband receiver of the PWI. Between 0714:45 UT and 0715:55 UT the receiver took data from the loop magnetic antenna in a frequency band below 11 kHz. The satellite was near its perigee, at altitudes slightly above 1 R_E on the nightside of the southern auroral zone. Figure 1 displays a frequency interval between 20 Hz and 1 kHz, where emissions were observed at the proton cyclotron frequency and its harmonics. We determine the proton cyclotron frequency (f_{H^+}) from the static magnetic field measured by the fluxgate magnetometer, and we plot the fundamental frequency and its harmonics up to the tenth as white dashed lines. At 0714:56 UT and at 0715:35 UT, intense bursty emissions are clearly visible near the proton cyclotron frequency. They last only about 2 s, and the corresponding peak in each of the frequency spectra lies close to f_{H^+} ($f_{H^+} \sim 100$ Hz and the frequency resolution of our analysis is 4 Hz). They are accompanied by weaker emissions near the second and third harmonics. Similar but even weaker waves are observed at 0715:08 and between 0715:26 and 0715:46. These spectral features are very like those reported previously for EIC waves [e.g., *Kintner*, 1980], except that here we find them in the spectra of magnetic field fluctuations; thus the observed emissions are not purely electrostatic.

[6] At higher frequencies (above ~300 Hz) the spectrogram shows emissions of auroral hiss. Their intensity is modulated with a period of 3 s, which is half the spin period of the satellite. (Note that the loop antenna measures a spin plane magnetic component.) Similar intense hiss is seen in the whole of the observed frequency band up to 11 kHz. After 0715:50 UT the hiss band has a sharp lower cutoff with a rising frequency; this feature belongs to a funnel-shaped auroral hiss emission which is detected during the next 3 min as the satellite moves toward the polar cap (not shown). Note that before 0715:00 the hiss emission exhibits stop bands around the fourth and fifth f_{H^+} harmonics, corresponding to another type of ion cyclotron frequency phenomenon similar to the ICH waves of *Kintner* [1980].

[7] During the time interval shown in Figure 1 the high-frequency waveform receiver (HFWR) of the PWI made full vector measurements of both the electric and magnetic wave fields. The waveforms were sampled at 4.46 kHz in snapshots lasting 0.459 s, once every 128.8 s. A snapshot was taken starting at 0715:41.61, designated by the box outlined in black in Figure 1. Waves near f_{H^+} and its second harmonic are apparent in Figure 1 at that time, though the peak intensity was observed about 7 s earlier. Unfortunately, the wave electric field was so intense and the event so short that the receiver electronics could not adjust the gain properly, with the result that the three electric channels were driven to saturation. The electric waveforms are thus clipped at about 20 mV/m, and we shall not use them for further analysis. The three magnetic waveforms show dominant fluctuations with a characteristic period of ~10 ms, on which higher-frequency waves are superposed. Our analysis of these vector measurements will be presented in section 3.

[8] To investigate the general features of the f_{H^+} emissions, we made a systematic search for similar cases during the lifetime of the PWI between March 1996 and September 1997. We used data recorded in the electromagnetic high-rate mode of the HFWR, with a sampling frequency of 71.4 kHz. The vector measurements of the electric and magnetic wave fields were made in snapshots of 0.445 s taken once every 9.2 s. This choice gave us a better chance of finding short-duration emissions than we would have had in the low-rate mode where the snapshots are separated by gaps of more than 2 min. Since f_{H^+} is too low to be detected by the HFWR during the apogee passes through the northern auroral zone, we searched for data near the perigee. Figure 2 shows the resulting orbital coverage. We found 44 perigee passes of the satellite through the southern auroral zone when the HFWR was in the high-rate mode. Of them, 15 orbits contained brief intervals of magnetic field fluctuations near f_{H^+} and sometimes also near its first few harmonics. These events were selected by examining the power spectra, using a criterion that a distinct peak must be present at a frequency between $0.8f_{H^+}$ and $1.5f_{H^+}$. They all occurred in the late afternoon, evening, and early morning sectors, but this grouping has no statistical significance; it could be just due to poor orbital coverage of the other MLT intervals by the HFWR high-rate data. The altitudes of the events range from 0.86 to 1.16 R_E. All of them were accompanied by emissions of auroral hiss at higher frequencies. Often these

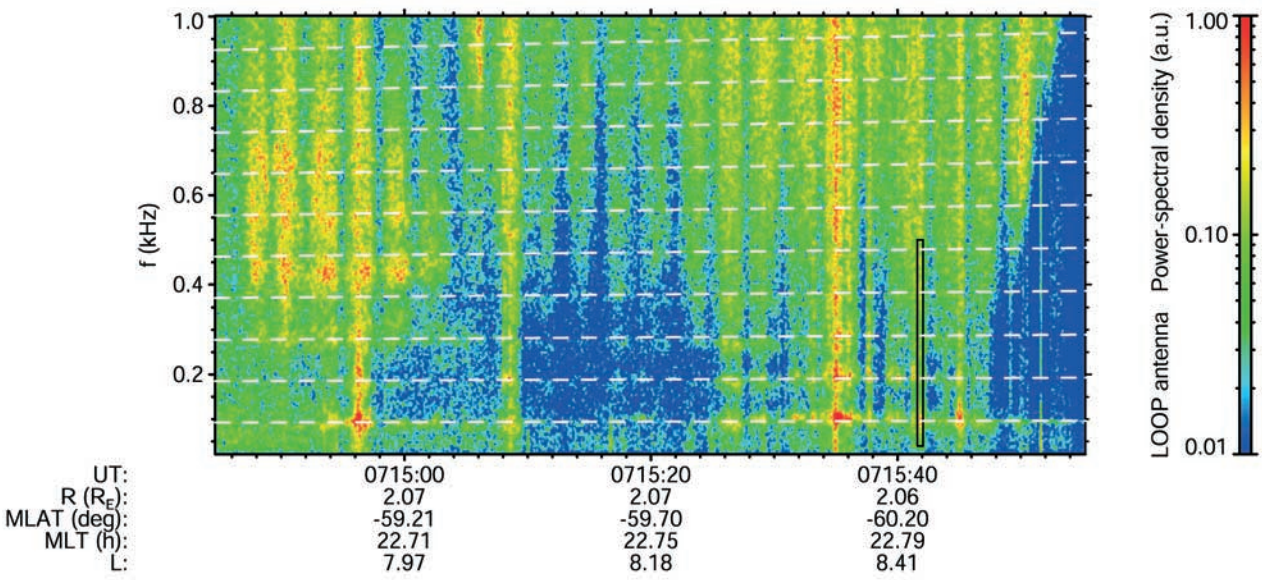

Figure 1. Time-frequency spectrogram of the magnetic field measured by the loop antenna on 5 June 1996.

f_{H^+} events were found in only one isolated snapshot or sometimes in a few snapshots per orbit, resulting in a total of 34 such events. Their duration in the spacecraft frame is comparable with or less than the time interval between successive snapshots; i.e., it is of the order of several seconds. We believe that this short duration probably reflects a spatial variability rather than a temporal variability; if so, the maximum transverse dimensions of the regions in which the waves propagate would be of the order of a few tens of kilometers.

3. Analysis Methods

[9] The methods we use to analyze the vector wave measurements are demonstrated in Figure 3. Here they are applied to the low-rate vector measurements mentioned in section 2, which were taken simultaneously with the data shown in Figure 1. It is worth noting that the search coil antennas were used in this case; so the presence of harmonic emissions is confirmed by data from an independent sensor system (recall that the loop antenna was used in Figure 1). This lessens the risk of experimental error, due, for instance, to break-through from the electric to the magnetic receiving channels in the presence of intense electric field fluctuations.

[10] Each component of the vector measurements is subjected to spectral analysis, and the resulting spectral matrices are subjected to further analysis as described in detail in Appendix A. To achieve fine frequency resolution, we divide each snapshot of waveform data into three parts with 50% overlap, we take the fast Fourier transform of each of these three waveform segments using the Hanning window, and the results are combined and averaged to estimate the spectral matrices (see Appendix A). In the low-rate mode the duration of each waveform segment is 0.23 s, which yields a frequency resolution of 4.4 Hz. Since only three spectral matrices are being averaged, the statistical errors of the spectral estimates are only reduced to about 40% [*Priestley*, 1989; *Press et al.*, 1992]. For the power spectra of the separate magnetic field components, this number directly shows us an estimate of the relative error. Its large value is an inevitable consequence of the required fine frequency resolution, given the experimental constraints.

[11] The power spectra of the magnetic field fluctuations in Figure 3a have peaks at f_{H^+} and $2f_{H^+}$; these are mainly seen in the components perpendicular to $\boldsymbol{B}_0$. The next two panels in Figure 3 present different aspects of the polarization of the wave magnetic field. The planarity of the polarization, as graphed in Figure 3b, was obtained from the singular value decomposition (SVD) of the magnetic spectral matrix (see Appendix A); evidently, at frequencies inside the peaks, the magnetic field fluctuations are almost confined to a plane. The other two parameters graphed in this

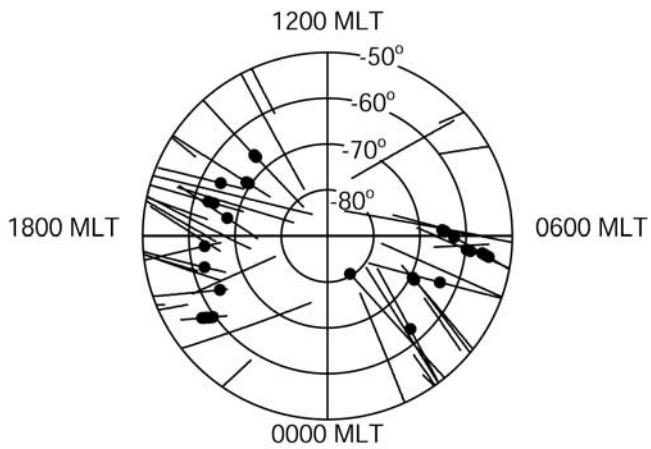

Figure 2. Southern perigee passes of the Polar spacecraft included in the systematic analysis. Parts of orbits are plotted by thick lines in the diagram MLT versus magnetic latitude for time intervals when the HFWR was in the high-rate telemetry mode. Solid circles indicate places where magnetic field fluctuations near f_{H^+} and harmonics were observed.

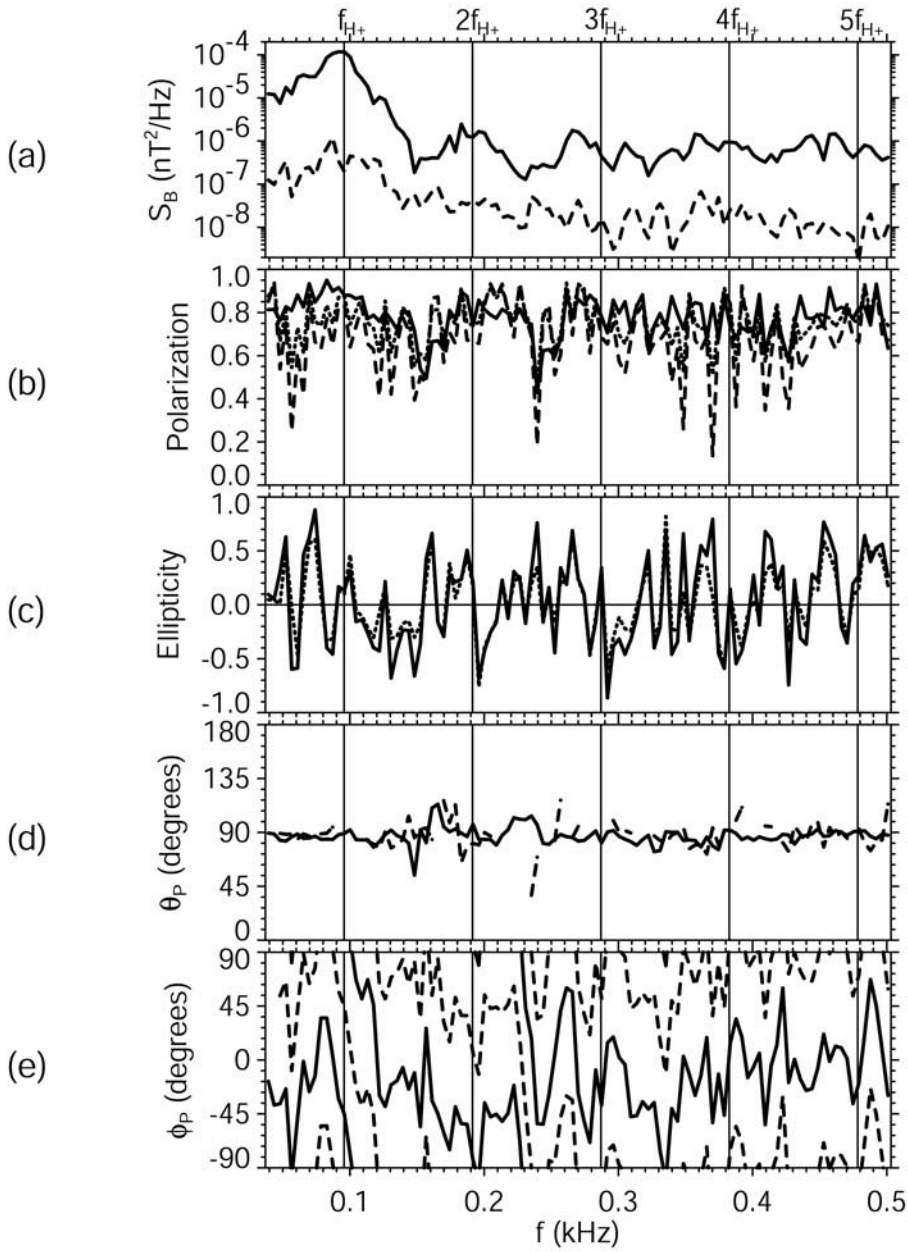

Figure 3. Analysis of the HFWR vector data recorded on 5 June 1996 around 0715:42 UT. (a) Solid line, sum of the power spectral densities of the two magnetic components perpendicular to $\boldsymbol{B}_0$; dashed line, power spectral density of the parallel magnetic component. (b) Solid line, planarity of polarization from singular values; dotted line, three-dimensional degree of polarization of *Samson and Olson* [1980]; dashed line, two-dimensional degree of coherence in the polarization plane using SVD. (c) Solid line, ellipticity from singular values; dotted line, ellipticity of *Samson and Olson* [1980]. (d) Solid line, angular deviation of the major axis of the polarization ellipse from $\boldsymbol{B}_0$; dashed line, the same angle for the minor axis. (e) Solid line, azimuth angle of the major axis of the polarization ellipse; dashed line, the same angle for the minor axis. Vertical lines are plotted at multiples of the proton cyclotron frequency.

panel characterize the coherence of the field components; both the three-dimensional (3-D) degree of polarization of *Samson and Olson* [1980] and the two-dimensional (2D) degree of coherence in the polarization plane are quite high, though less than unity. Further interesting results are obtained from the determination of the sense of the elliptic polarization with respect to $\boldsymbol{B}_0$. In Figure 3c this parameter is combined with the ratio of the two axes of the polarization ellipse. A value near -1 means left-hand circular polarization, a value near +1 means right-hand circular polarization, and 0 represents linearly polarized waves. Again we use both the SVD method (see Appendix A) and the method of *Samson and Olson* [1980], with very similar results. The sense of polarization fluctuates between right handed and

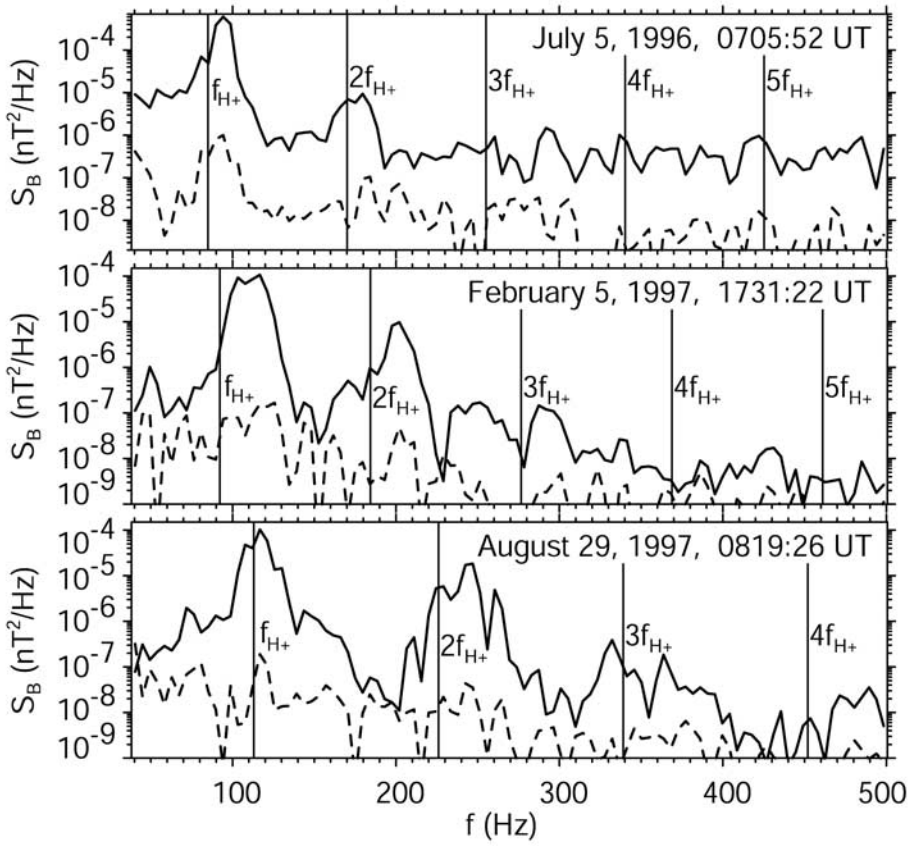

Figure 4. (top) Spectra of the magnetic field observed on 5 July 1996 around 0705:52 UT. (middle) Spectra observed on 5 February 1997 around 1731:22 UT. (bottom) Spectra observed on 29 August 1997 around 0819:26 UT. Solid line, sum of the power spectral densities of the two magnetic components perpendicular to $\boldsymbol{B}_0$; dashed line, power spectral density of the parallel magnetic component.

left handed at frequencies inside the peaks at f_{H^+} and its second harmonic. The polarization is often far from being linear, with ellipticities above +0.2 or below −0.2.

[12] When the magnetic field polarization is elliptic, we can determine the directions of the two axes of the polarization ellipse. Figures 3d and 3e show two angles that define these directions in a spherical coordinate system linked to $\boldsymbol{B}_0$: they are the angular deviation from $\boldsymbol{B}_0$ (θ_P) and the azimuth angle (ϕ_P), respectively. The azimuth is measured from the plane of the local magnetic meridian, with the direction of increasing L value at 0°, and an increase in azimuth corresponds to a right-handed rotation around $\boldsymbol{B}_0$. Since each polarization axis has two indistinguishable ends, its direction can be given in one hemisphere only. Here we have chosen to define it in the hemisphere where $0° \leq \theta \leq 180°$ and $-90° \leq \phi < 90°$. If the polarization is close to linear, only the direction of the major axis is determined. At frequencies inside the peaks near f_{H^+} and $2f_{H^+}$, both the major axis (solid line) and the minor axis (dashed line) are found to be almost perpendicular to $\boldsymbol{B}_0$ ($\theta_P \sim 90°$). The same results are obtained at higher frequencies for auroral hiss. The azimuth, however, is highly variable as a function of frequency, the minor axis always being ~90° off with respect to the major axis; needless to say, it would be exactly 90° off if the polarization ellipse were exactly perpendicular to $\boldsymbol{B}_0$. In the rest of this paper, the properties of the wave magnetic field graphed in Figures 3b through 3e will be referred to collectively as the polarization parameters.

[13] The 34 sets of measurements made in the electromagnetic high-rate mode of the HFWR (Figure 2) are used for the systematic analysis presented in section 4. The analysis methods we use are similar to those presented above, though with some differences of detail, both in how the calculations are performed and in how the results are displayed. As regards the raw data, the only differences are the slightly shorter duration of the high-rate snapshots, the shorter interval between successive snapshots, and the much higher sampling frequency (see section 2). For the spectral analysis, we again divide the snapshot into three waveform segments with 50% overlapping; the duration of each segment is 0.22 s, and the resulting frequency resolution is 4.5 Hz. The results from three such analyses are displayed in Figure 4, in the same way as in Figure 3a. Then for each of the 34 spectra, we note the following quantities: the frequency of the main peak near f_{H^+} at this peak, the maximum value of the spectral density, and the width of the peak at the level of 25% of the maximum. Next, the polarization parameters that were graphed in Figures 3c–3e are calculated as described above, but only over the frequency range between these limits of the peak width. On the other hand, the three parameters that were graphed together in Figure 3b are now calculated differently, in a way that reduces the statistical errors of their estimates: each

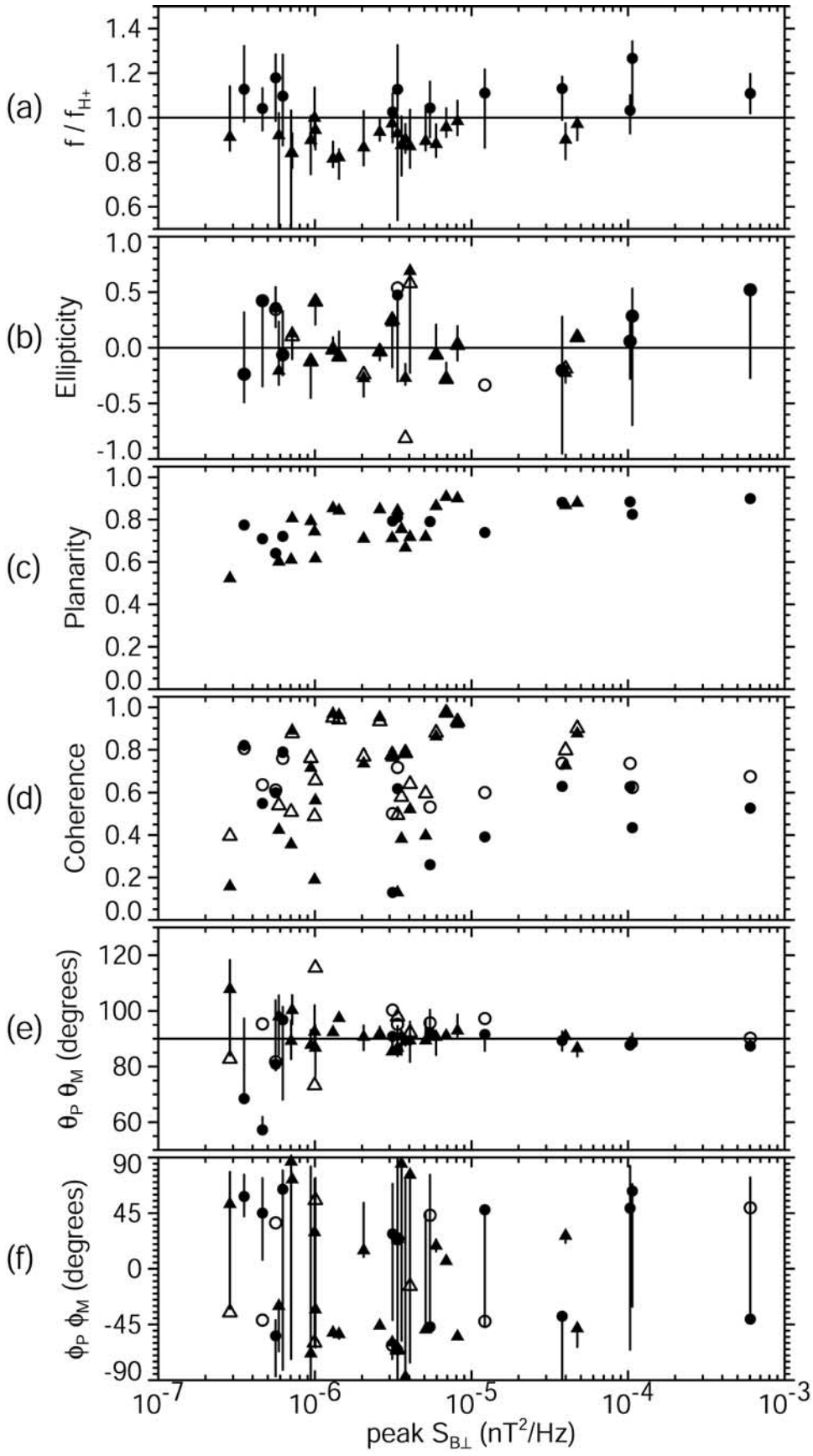
(a)
f / f_H+
1.4
1.2
1.0
0.8
0.6
(b)
Ellipticity
1.0
0.5
0.0
-0.5
-1.0
(c)
Planarity
1.0
0.8
0.6
0.4
0.2
0.0
(d)
Coherence
1.0
0.8
0.6
0.4
0.2
0.0
(e)
θP θM (degrees)
120
100
80
60
(f)
φP φM (degrees)
90
45
0
-45
-90
10^-7
10^-6
10^-5
10^-4
10^-3
peak SB⊥ (nT²/Hz)

spectral matrix is averaged over the frequency range between the 25% level limits, and from these averaged spectra we compute the parameters concerned. Finally, for a synoptic view of the entire set of results, the frequency and width of the main peak, along with the polarization parameters for the waves within this peak, are displayed in Figure 5 versus the peak spectral density. The reason for displaying them in this way is that the results from the analyses of the strongest waves are likely to be the most significant, since they are the ones least affected by noise. Note that the three parameters just mentioned, which were graphed together in Figure 3b (labeled polarization), are graphed in Figure 5 in two separate (Figures 5c and 5d, labeled planarity and coherence). All of these results will be discussed in the next section.

4. Analysis Results

[14] Power spectra of three specimens of the high-rate data are shown in Figure 4. In all these cases the waveforms of the magnetic field show distinct fluctuations with a period of ~10 ms, corresponding to the main peak observed in each spectrum near f_{H^+}. For the event of 5 July 1996, recorded at 2013 MLT, the waveforms also contain much faster fluctuations related to an auroral hiss emission extending up to 10 kHz. The dominant feature in each spectrum, however, is the peak at a frequency of $1.1f_{H^+}$ (f_{H^+} = 85 Hz is determined from a local measurement of the static magnetic field by the fluxgate magnetometer). Another peak near $2f_{H^+}$ is also clearly visible. Both peaks are mainly seen in the components perpendicular to $\boldsymbol{B}_0$. The same holds true for the spectra recorded on 5 February 1997 at 0535 MLT (f_{H^+} = 92 Hz) showing the main peak located at $1.3f_{H^+}$ and the secondary peak located above $2f_{H^+}$. In the spectra recorded on 29 August 1997, at 1448 MLT, the main peak is located just above f_{H^+} (f_{H^+} = 113 Hz in this case). The waveforms also contain faster fluctuations, notably with a period of around 5 ms. These correspond to the intense peak near and above $2f_{H^+}$ seen in the spectrum of the perpendicular components.

[15] The polarization of the magnetic field has been investigated for all 34 events shown in Figure 2. We have focused our attention on the frequencies around the main peak near f_{H^+}, because often the secondary peaks are invisible or are too weak for analysis. In cases where we see sufficiently intense peaks near $2f_{H^+}$ (such as the cases shown in Figure 4), the analysis near $2f_{H^+}$ gives results similar to those for the main peak near f_{H^+}. Figure 5 displays the results as a function of the peak spectral density. Note that the three examples shown in Figure 4 are the most intense cases, represented by the three rightmost points in Figure 5. Note also that the case shown in Figure 3 has not been included in this systematic analysis (neither in Figure 2 nor in Figure 5) because the instrument was then operating in a different mode. The weakest events that we are able to detect have spectral densities between 3×10^{-7} and 10^{-6} nT^2/Hz. This limitation is caused by the noise on the search coil antennas, which is much less at high frequencies (of the order of 10^{-10} nT^2/Hz at 1 kHz) but rapidly increases at lower frequencies. At the lower edge of the frequency interval considered in this study (~70 Hz), the noise increases up to 5×10^{-8}–10^{-7} nT^2/Hz (G. Hospodarsky, private communication, 2001).

[16] Figure 5a shows, for each event, the frequency of maximum spectral density (solid symbols) and the widths of the peak at the level of 25% of the maximum (vertical line). Of the 34 events, 12 have their main peak above f_{H^+} (circles) while 22 have it below f_{H^+} (triangles). Most of the peaks contain f_{H^+} within their width at the 25% level. The median width at this level is $0.2f_{H^+}$. If the level defining the peak width were lowered to 10% of the maximum, the median width would increase to $0.34f_{H^+}$. The frequency resolution of the analysis (4.5 Hz) is about 5% of f_{H^+}. This resolution sets a lower limit to the peak width that can be determined from this data set.

[17] Figure 5b shows the ellipticity obtained by the same analysis methods as in Figure 3c. The open symbols represent the results of the method of *Samson and Olson* [1980] at the frequency of the maximum spectral density. The solid symbols represent the SVD results at the same frequency (when only a solid symbol is visible, it means that the results of the two methods are almost the same). Vertical lines are drawn between the minimum and maximum SVD ellipticities encountered at frequencies within the peak width at the 25% level. Since the ellipticity has little meaning unless the signals are related somehow, we plot the results of the method of *Samson and Olson* [1980] only when the 3-D degree of polarization as defined by these authors (see below) is larger than 0.6 for the same case. The choice of this value is connected to the asymptotic value of the 3-D degree of polarization for isotropic noise discussed later in section 5. Similarly, the results of the SVD method are plotted only when the 2-D degree of coherence in the polarization plane is larger than 0.4. An important point for the identification of the possible modes of propagation is that there is no systematic trend for peaks above f_{H^+} (circles) and below f_{H^+} (triangles) to have either right-hand or left-hand elliptic polarization; both polarization senses are encountered regardless of the frequency. Moreover, the polarization is either very close to linear or it fluctuates widely between the two senses of elliptic polarization; an example of the latter behavior is shown in Figure 3c.

[18] The planarity of the magnetic field polarization is shown in Figure 5c. To decrease the statistical errors of the spectral estimates, the spectra were averaged over the entire frequency range within the peak width at 25% of the

Figure 5. (opposite) Summary of 34 cases of magnetic field fluctuations near f_{H^+}. (a) Peak frequency and width with respect to f_{H^+}. (b) Solid symbols, ellipticity from the SVD; open symbols, ellipticity of *Samson and Olson* [1980]. (c) Planarity from the SVD. (d) Solid symbols, coherence in the two-dimensional polarization plane using the SVD; open symbols, three-dimensional degree of polarization of *Samson and Olson* [1980]. (e) Angular deviation θ of axes of polarization ellipse from $\boldsymbol{B}_0$: solid symbols, major axis; open symbols, minor axis. (f) Azimuth angle ϕ of axes of polarization ellipse from $\boldsymbol{B}_0$: solid symbols, major axis; open symbols, minor axis. Vertical lines are minimum-maximum intervals encountered at frequencies within the peak width at 25% of the maximum. Circles, peaks above f_{H^+}; triangles, peaks below f_{H^+}.

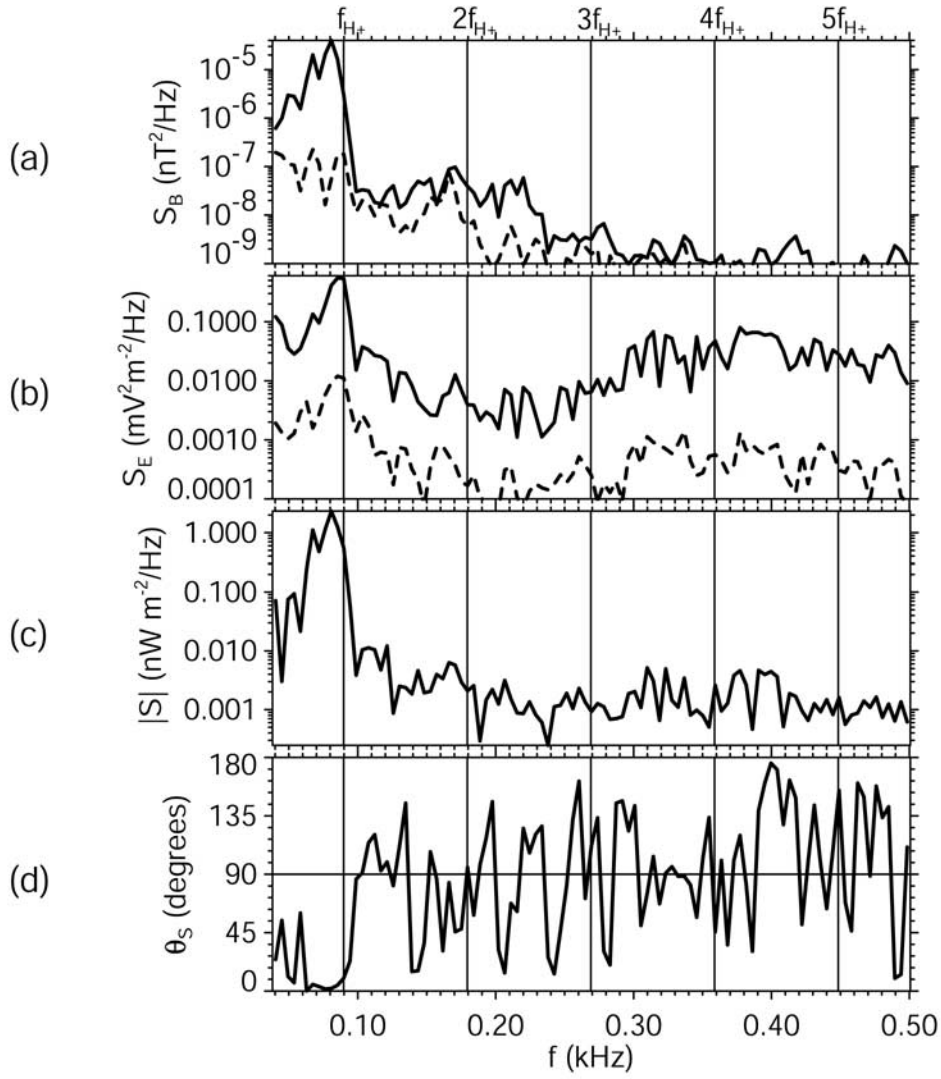

Figure 6. Analysis of electromagnetic waves observed on 5 July 1996 around 0707:15 UT. (a) Solid line, sum of the power spectral densities of the two magnetic components perpendicular to $\boldsymbol{B}_0$; dashed line, power spectral density of the parallel magnetic component. (b) Solid line, sum of the power spectral densities of the two electric components perpendicular to $\boldsymbol{B}_0$; dashed line, power spectral density of the parallel electric component. (c) Spectral density of the Poynting flux. (d) Angular deviation of the Poynting flux direction from $\boldsymbol{B}_0$.

maximum. A single value of the planarity for each event was then estimated by the SVD procedure described in Appendix A. Triangles again represent peaks below f_{H^+}, while circles correspond to peaks above f_{H^+}. For the most intense peaks the planarity is quite close to 1, which means that the magnetic field is well confined to a plane. Only the cases with the least intense peaks, just above the noise limit, have planarities less than 0.65.

[19] The coherence of the polarization is displayed in the same way in Figure 5d. The open symbols give the 3-D degree of polarization of *Samson and Olson* [1980], and the solid symbols give the 2-D degree of coherence in the polarization plane. Again, both values were obtained from spectra averaged over the peak width. The results cover a wide range, from 0.1 to nearly 1. For the intense cases, the values of the coherence mostly lie between 0.3 and 0.9.

[20] The directions of the axes of the polarization ellipse are shown in Figures 5e–5f; we use the same spherical coordinates as in Figures 3d–3e. The results for the minor axis are represented by open symbols. They are not plotted for events with low ellipticity (between −0.3 and +0.3) because for polarizations close to linear the direction of the minor axis is ill defined. The direction of the major axis is represented by solid symbols, with vertical lines indicating the ranges of variation at frequencies within the peak width at 25% of the maximum. The angular deviation from $\boldsymbol{B}_0$ (θ_P) always lies within a few degrees of 90°, except for weak cases below 10^{-6} nT^2/Hz. Similar values are obtained for both axes, sometimes with slightly larger deviations of the minor axis. These results express an important general property of the magnetic field polarization: the magnetic fluctuations are confined close to the plane perpendicular to

$\boldsymbol{B}_0$. The results for the azimuth angle ϕ_P do not exhibit any significant clustering with respect to the plane of the local magnetic meridian. Hence it is likely that the main direction of polarization (i.e., the direction of the major axis) is distributed randomly over all the azimuth angles around the $\boldsymbol{B}_0$ direction.

[21] Besides the waveforms of the magnetic field components analyzed above, those of the three electric field components were measured simultaneously for all of the events. However, since the automatic gain control was based on the average values seen in the previous snapshot (a case in point is shown in Figure 3), in 70% of the cases the intense electric field of these short-lived phenomena saturated the electric channels of the receiver. Thus in a typical event, the amplitude of the electric field fluctuations is above the usual saturation level for these cases (around 20 mV/m). Since the average power spectral density for the most intense case of magnetic field fluctuations near is 3×10^{-4} nT^2/Hz and the bandwidth of the peak is around 20 Hz, we find the maximum root-mean-square value (B) of the modulus of the magnetic field vector to be approximately 0.06 nT. Knowing that the corresponding values of the electric field vector (E) exceed 20 mV/m in 70% of all cases, it follows that the ratio E/B is usually greater than the speed of light c. Note that c is being used here only as a physical normalization for comparing the obtained values with the results of *Mozer et al.* [1997] and *Chaston et al.* [1998] and that the above estimate is very rough. Note also that this estimate is only a lower limit of the possible E/B values, and from the distribution of the peak magnetic power spectral density in Figure 5 we conclude that a typical E/B could be at least 1 or 2 orders of magnitude greater than c.

[22] For 10 of the 34 events the electric waveforms are not clipped, and all six electromagnetic components can be used in the analysis. Clearly, this subset of cases is not representative because it only includes events where E is weaker than $\sim$20 mV/m, while no condition is imposed on the magnetic field by that selection. In all these cases the main peak in the magnetic spectrum is below f_{H^+}, and in all but one the peak spectral density is relatively low, less than 10^{-5} nT^2/Hz. In seven cases the main peak in the electric field spectrum is very weak (E/B is no more than a few hundredths of c) and/or it occurs at a frequency different from that of the main peak in the spectrum of the perpendicular magnetic components (probably due to the simultaneous presence of electrostatic emissions), but in three cases the main peak in the magnetic spectrum has a clear counterpart at the same frequency in the electric spectrum. Of these three, Figure 6 shows the one in which the electric field is the most intense. The main peak in the spectrum of the perpendicular magnetic components occurs just below f_{H^+} (Figure 6a) and a similar peak is observed in the spectrum of the perpendicular electric components (Figure 6b) but at a frequency about 5–10% higher. This difference is unremarkable, since there are no grounds for thinking that the ratio of E to B should be independent of frequency; if nevertheless we compare the peaks of the two spectra, we find that the E/B ratio is approximately $0.4c$. The maximum amplitude of the electric field fluctuations is around 10 mV/m, which is about half the saturation level. The intensities of the electric spectra increase with frequency above $\sim$300 Hz, owing to the presence of auroral hiss.

[23] Inside the peak near f_{H^+}, both the electric and the magnetic fields are polarized in a plane close to perpendicular to $\boldsymbol{B}_0$, and the angle between their major polarization axes is approximately 90° (not shown). Having full vector measurements of both fields, we can calculate the vector of the mean Poynting flux as the average of $\boldsymbol{S} = \boldsymbol{E} \times \boldsymbol{B}/2\mu_0$, where μ_0 is the vacuum permeability. Figure 6c shows that the electromagnetic emission near f_{H^+} corresponds to a large peak in the spectral density of the modulus of $\boldsymbol{S}$, attaining $\sim$2 nW m^{-2}/Hz. The direction of $\boldsymbol{S}$ is characterized by its angular deviation from $\boldsymbol{B}_0$ shown in Figure 6d. The results show that the Poynting flux is directed along $\boldsymbol{B}_0$ in the peak near f_{H^+}. In the southern auroral zone this means that the waves are propagating upward.

5. Interpretation

[24] The observed polarization of the perpendicular magnetic field fluctuations is often clearly elliptic, and both left-hand and right-hand senses can be encountered (see Figures 3c and 5b) with no correlation to the position of the peak relative to f_{H^+}. *Temerin and Lysak* [1984] reported a similar polarization for the electric field of waves observed between the multi-ion hybrid frequency and f_{H^+}. Assuming that cold plasma wave theory applies, these waves were propagating in the R mode below the multi-ion crossover frequency and in the ion cyclotron L mode above the crossover. If the observed field had been that of a single plane wave in either of these modes, propagating not far from the resonance cone, the polarization should have been linear. This was not observed, and the explanation of *Temerin and Lysak* [1984] for this apparent contradiction was that the observations are probably best interpreted as the superposition of multiple linearly polarized waves with different phases; as proposed by *Chaston et al.* [1998], this could also be the case for the f_{H^+} waves.

[25] Since we could not realistically suppose a simple case with only a few superposed waves where the polarization properties could be easily found, we ran a simulation with a large number of waves, all linearly polarized. Our procedure was like the one used in the simulation of stationary signals by *Anderson et al.* [1996]. In each realization of the waveforms of the three magnetic components, we summed simulated signals at several discrete frequencies in a predefined frequency band and a wide-band Gaussian noise. At each frequency, we summed 100 elementary sine waves, all with predefined amplitudes. Each elementary wave was linearly polarized in the plane perpendicular to $\boldsymbol{B}_0$ at a random azimuth and had a random initial phase. The resulting magnetic waveforms were

$$
\begin{aligned}
B_1(t) &= \frac{N}{Q}\,\sigma_1(t) + \sum_{j=-M}^{M} A_j \sum_{i=1}^{N} \cos\phi_{ij} \sin\left(2\pi f_j t + \alpha_{ij}\right) \\
B_2(t) &= \frac{N}{Q}\,\sigma_2(t) + \sum_{j=-M}^{M} A_j \sum_{i=1}^{N} \sin\phi_{ij} \sin\left(2\pi f_j t + \alpha_{ij}\right) \qquad (1) \\
B_3(t) &= \frac{N}{Q}\,\sigma_3(t),
\end{aligned}
$$

where $B_1(t)$ and $B_2(t)$ are the perpendicular components of the magnetic field fluctuations, $B_3(t)$ is the parallel

component, f_j is the frequency, and t is time; $\sigma_1(t)$, $\sigma_2(t)$, and $\sigma_3(t)$ are three realizations of random noise with a Gaussian distribution and unit variance, while Q we call the signal quality parameter; ϕ_{ij} and α_{ij} are the azimuth and the initial phase of the ith wave at the jth frequency, respectively. For given i and j, these angles are constant, not varying with time. On going from one i or j to the next, their new values are generated as random variables with uniform distributions over the interval $\langle 0, 2\pi \rangle$. This process is repeated for $N = 100$ elementary waves. The frequencies f_j and amplitudes A_j are chosen to match average properties of experimental data from the set presented in Figure 5. The interval between two neighbor frequencies $f_{j+1} - f_j$ is a constant defined by the frequency resolution of the spectral analysis described in section 3, i.e., $f_{j+1} - f_j = 1/T = 4.5$ Hz, where $T = 0.22$ s is the duration of each segment of the analyzed high-resolution waveform. The amplitudes A_j are defined to simulate a representative peak near f_{H^+},

$$A_j = \exp\left[-\frac{(f_j - f_0)^2}{\delta^2} \right], \qquad (2)$$

where f_0 is the central frequency of the peak, chosen at $f_0 = 100$ Hz, and δ is the peak half width, chosen at an average experimental value of $\delta = 14$ Hz. The total frequency band included in the simulation is chosen to cover the frequency interval $\langle f_0 - 2\delta, f_0 + 2\delta \rangle$. Accordingly, $M = 6$ and we sum the signals at 13 frequencies. The waveforms simulated as described by (1) were subjected to spectral analysis, and the same wave field parameters as are graphed in Figure 5 were calculated by the same methods, described in sections 3 and 4. This procedure was repeated for 50 independent realizations of the signals B_1, B_2, and B_3, and from the resulting statistical data set we calculated the mean value and the standard deviation of each parameter, as estimates of what the corresponding means and standard deviations would be if the data set were infinite.

[26] The results are shown in Figure 7, in a format similar to that of the experimental results in Figure 5. The simulated ellipticity at the frequency of the peak maximum (Figure 7a) always has a mean value close to zero, and the standard deviation is about 0.4 (only slightly higher for noisy data), consistent with results in Figure 5b.

[27] The simulation of planarity estimates (Figure 7b) follows the procedure used previously in Figure 5c; to increase the statistical significance of the results, we average all the simulated spectral matrices in the frequency band defined by the width of the peak at 25% of the maximum power, i.e., five matrices for the above choice of δ. At high Q the planarity is equal to 1, since the magnetic field of the simulated waves fluctuates only in the two perpendicular components. At high levels of noise (low Q), the planarity estimate decreases to an asymptotic mean value of 0.4 with a standard deviation of 0.1. This is a consequence of the method of spectral analysis where we average only a small number of spectral matrices. If this number tended to infinity, the asymptotic mean value for uncorrelated noise would tend to 0.

[28] Neither of the two estimates of coherence (Figure 7c) shows a clearly significant decrease with increasing level of noise. This behavior is due to a combination of two effects, one at low and one at high Q. For low Q the simulation gives the asymptotic mean values as ≈ 0.4 for the coherence in the 2-D plane of polarization and ≈ 0.6 for the 3-D degree of polarization of *Samson and Olson* [1980], with standard deviations of ≈ 0.1 in both cases. Those values are again a consequence of averaging only a small number of spectral matrices, and both of them would become zero asymptotically if this number tended to infinity. For high Q, we obtain slightly higher asymptotic mean values of ≈ 0.5 and ≈ 0.8 with a similar standard deviation. The effect playing the principal role here is the mixing of several frequencies with random phases in the analyzed waveform (1). At each of these frequencies separately, the contribution to the waveform is perfectly coherent, and if we set $M = 0$ in (1), we get both coherence estimators equal to 1 at high Q (not shown).

[29] The average directions of the axes of the polarization ellipse (Figures 7d–7e) stay in the plane perpendicular to $\boldsymbol{B}_0$, but for high noise levels they fluctuate significantly, the standard deviation being higher for the minor axis (Figure 7e). This asymptotic behavior for high Q is a trivial consequence of the presence of the simulated signal only in the two perpendicular components. In the limit where only isotropic noise is present (low Q), we can suppose that the directions of the polarization axes have a uniform distribution on the surface of a unit sphere. A simple calculation shows that the theoretical mean value of θ for this distribution is $\pi/2$ and the standard deviation is $(\pi^2/4 - 2)^{1/2} \approx 39°$. Those values agree well with the simulation results at low Q. The simulation also gives us the azimuth angle ϕ_P which for both axes is distributed randomly in the interval $\langle 0, 2\pi \rangle$ (not shown).

[30] Note that the dependence of these various parameters on the signal quality parameter Q is quite like that seen in Figure 5. When the signal intensity $S_{B\perp}$ in Figure 5 decreases near the noise level (which, we recall, was of the order of 10^{-7} nT^2/Hz for the experimental data shown in Figure 5), the parameters start to fluctuate over more or less the same ranges as in these simulations, and the planarity, on the average, decreases to values similar to those in Figure 7b.

[31] The only polarization parameter in Figure 5 that is not very well reproduced by the simulation is the coherence (Figure 5d): for weak signals, the observed coherence varies over a wider range than the simulation predicts. One reason probably has to do with variations of the peak width in the experimental observations, given that the coherence estimate depends on the frequency range over which the spectral matrix is averaged before the analysis begins. Recall that we have chosen, for the half-width δ of the simulated peak, a fixed value equal to the median of the observed widths, but in reality the widths of the peaks near f_{H^+} vary from one observation to another (see Figure 5a). Since the coherence, like the planarity, is calculated from a matrix averaged over the band between the 25% level limits on either side of the peak (see section 3), variations of the peak width affect the experimental values of the coherence. Another possible reason is that, contrary to an assumption made in our model of the wave field, the statistical distribution of the elementary waves in azimuth may not be uniform. If, instead, their directions of propagation were clustered in azimuth, then the coherence would be enhanced. In the limit where all the waves were propagating in the same direction, both measures of the coherence would

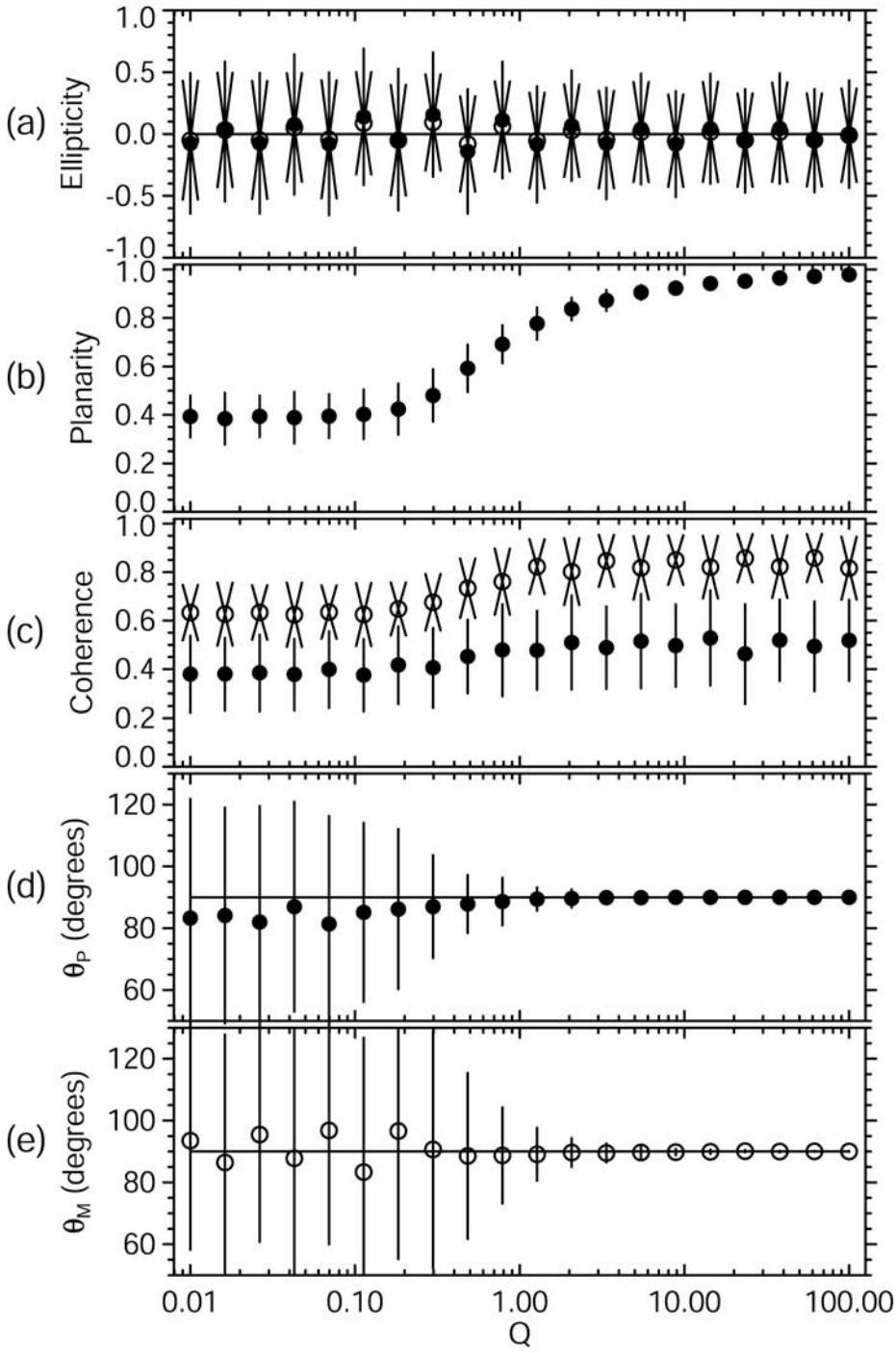

Figure 7. Analysis of simulated data as a function of the signal quality parameter (Q). Circles represent an estimate of the mean value; error bars show an estimate of the standard deviation. (a) Solid symbols (error bars as vertical lines), ellipticity from the SVD; open symbols (error bars as two crossed oblique lines), ellipticity of *Samson and Olson* [1980]. (b) Planarity from the SVD. (c) Solid symbols (vertical lines), coherence in the two-dimensional plane of polarization obtained from the SVD; open symbols (two crossed oblique lines), three-dimensional degree of polarization of *Samson and Olson* [1980]. (d) Angular deviation θ_P of the major axis of the polarization ellipse from $\boldsymbol{B}_0$. (e) Similar angle θ_M for the minor axis.

be 1 and the polarization would be linear. An inspection of the data suggests that both of these effects are acting: the higher-than-expected values of the coherence occur when the spectral peak is narrow or when the ellipticity is low.

[32] Finally, we recognize that from the polarization and coherence analyses alone we cannot exclude the further possibility of the superposition of elliptically polarized waves. Indeed, the frequent presence of a small but nevertheless significant component of the wave magnetic field parallel to $\boldsymbol{B}_0$, as typified by the data of Figures 3 and 4, implies that the polarization of the elementary waves must be elliptical to some extent; this statement, however, assumes that the plasma can be treated as collisionless and cold, which is unlikely to be the case in the auroral region. On the evidence, wave modes with both left-hand and right-hand polarization would have to exist both below and above f_{H^+} (see the discussion in section 6). There is also a physical argument suggesting that such modes are probably not generated in the auroral region. The elliptical polarization in a plane close to perpendicular to $\boldsymbol{B}_0$ implies a wave vector nearly parallel to $\boldsymbol{B}_0$, unlike the linear polarization in the same plane where the wave vector can also be perpendicular to $\boldsymbol{B}_0$. If the electric field fluctuations are also close to perpendicular to $\boldsymbol{B}_0$ (which is suggested by our observations where the electric field measurements are available), then the electric field is also perpendicular to the wave vector and the E/B values give us the phase speeds. For a wave resonant with a typical 1-keV electron beam, the phase speed would be $\approx 2 \times 10^7$ m/s, which is smaller than the observed E/B values by at least an order of magnitude. For ion beams of similar energies this difference is even larger.

6. Discussion and Conclusions

[33] We have reviewed our observations of magnetic-field fluctuations near f_{H^+} and its lowest harmonics in the data of the Plasma Wave Instrument on the Polar spacecraft. So far as we know, this is the first systematic study of such events (apart from the case study by *Chaston et al.* [1998]). Though relevant electric field data have been studied extensively in the past, the corresponding magnetic fields had not previously been investigated in detail, probably due to a lack of suitable measurements. By means of a numerical simulation, we have demonstrated that the observed sense of polarization and ellipticity are statistically very similar to the results of superposing many linearly polarized waves, with their directions of polarization distributed randomly in the plane perpendicular to $\boldsymbol{B}_0$.

[34] The simplest hypothesis about the propagation mode of these electromagnetic emissions might be one based on cold plasma theory [*Stix*, 1992]. The waves could be generated as electrostatic near f_{H^+} and its lowest harmonics [e.g., *Cattell et al.*, 1998] and then be refracted to much longer wavelengths where electromagnetic cold plasma modes exist, as was suggested for similar cases at higher frequencies by *Kintner* [1992]. The frequency spectra would reflect the original electrostatic waves, but the observed waves would be propagating in a cold plasma electromagnetic mode. The main problem with this hypothesis is that, above f_{H^+}, we observe both left-hand and right-hand elliptically polarized waves with their magnetic field fluctuations close to the plane perpendicular to $\boldsymbol{B}_0$, an observation that we have modeled by summing multiple linearly polarized waves. The sole electromagnetic cold plasma mode just above f_{H^+} is the whistler mode which has right-hand circular polarization for parallel wave vectors; moreover, with increasing angular deviation between the wave vector and $\boldsymbol{B}_0$, the magnetic field polarization becomes more and more linear and closer to the direction of $\boldsymbol{B}_0$. This is in clear contradiction with the observed polarization of the magnetic field fluctuations, whether the latter is taken at its face value or interpreted in terms of our model. Just below f_{H^+}, on the other hand, there is the electromagnetic ion cyclotron mode [*Temerin and Lysak*, 1984] which has a resonance cone, and it is possible that the waves were propagating in this mode close to the resonance. If so, then we must suppose that the waves observed above f_{H^+} were generated below f_{H^+} in the plasma and were shifted by the Doppler effect to frequencies above f_{H^+} in the frame of the orbiting spacecraft; the apparent continuity of the spectra through f_{H^+} argues in favor of this view (see Figures 3, 4, and 6).

[35] Further light was shed on the mode of propagation by a study of the waves at the harmonics of f_{H^+}. Their generation must have involved kinetic effects, since cold plasma theory predicts no significant effects at harmonics of the ion cyclotron frequencies. Here again, though, the waves might have traveled away from their source region and been converted into a cold plasma mode in which they were observed. We examined this possibility by calculating the polarization parameters for the waves in the peak near the second harmonic, in every case among the 34 events where this peak was visible in the spectra. In all such cases, these parameters were similar to the ones found for the fundamental; see Figure 3 for an instance. This finding is incompatible with propagation in the whistler mode, which is the only cold plasma mode existing at the second harmonic of f_{H^+}. Cold plasma theory is thus inadequate to explain the propagation of the second-harmonic waves, and we must take into account thermal effects [e.g., *Stix*, 1992; *André*, 1985]; hence these effects may be important for waves in the peak near f_{H^+} also.

[36] Direct calculation of the Poynting vector from vector measurements of three magnetic and three electric components was not done systematically for all the cases. We are therefore unable to draw more general conclusions, but for one selected case the Poynting flux was upgoing and approximately parallel to the $\boldsymbol{B}_0$ direction. This result is in agreement with *Chaston et al.* [1998] and has implications for the possible generation mechanisms.

[37] Progress in identifying the modes of generation and propagation of these electromagnetic waves requires a correct model of the plasma based on direct measurements in the auroral zone, where often the dominant components of electron and ion distributions are beams. Indeed, these regions have been demonstrated (e.g., recently by *Mc Fadden et al.* [1999]) to be devoid of low-temperature plasma. Such plasma conditions can make the ion cyclotron waves unstable, as has been demonstrated in the electrostatic approximation, e.g., by *Bergmann* [1984], *Bergmann and Hudson* [1987], *Kintner et al.* [1978], and *Cattell et al.* [1998]. It has also been shown that the short-wavelength EIC waves can be shifted in frequency by the Doppler effect

owing to the spacecraft motion. Measurements of the particle distributions are thus needed in order to study in detail both the real and the imaginary parts of the dispersion relation of the observed waves and their E/B ratio. We are pursuing analysis of supporting plasma data and will report the results when they become available.

[38] Meanwhile, we summarize our principal conclusions:

1. In the auroral zone, peaks near f_{H^+} and its lowest harmonics are observed in the magnetic power spectra. The main peak can be either slightly below or slightly above the local f_{H^+}. The E/B ratio is usually higher than the speed of light, suggesting that we observe a magnetic component associated with the traditional EIC waves. We found these electromagnetic waves in about a third of the examined orbits when the Polar spacecraft was passing through the southern auroral zone at an altitude of $\sim 1\ R_E$.

2. The magnetic field fluctuations are close to the plane perpendicular to $\boldsymbol{B}_0$. The polarization ranges from left-hand elliptic through linear to right-hand elliptic, both below and above f_{H^+}. The observed directions of the major polarization axis are not clearly organized with respect to the local magnetic meridian.

3. The observed polarization can be explained by the superposition of many linearly polarized waves close to the plane perpendicular to $\boldsymbol{B}_0$. This is our main result.

4. To fully explain the observed polarization of the magnetic field fluctuations, at the harmonics as well as at the fundamental proton cyclotron frequency, a kinetic approach is essential.

Appendix A: Singular Value Decomposition of the Magnetic Spectral Matrix

[39] To determine the polarization of the magnetic field fluctuations, we use a method that was developed originally for direction finding in the frequency domain and is based on the singular value decomposition of the magnetic spectral matrix [*Santolík et al.*, 2002]. It uses Faraday's law and assumes the presence of a single plane wave. This assumption does not apply in our particular case, but nevertheless the method yields estimates of the lengths and directions of the axes of the polarization ellipsoid.

[40] The first step in this analysis method is spectral analysis of the magnetic field vector. At a given frequency, we estimate values B_i proportional to the complex amplitudes of the three Cartesian components. We use a procedure based on the fast Fourier transform (FFT), and we put the results in a coordinate system linked to $\boldsymbol{B}_0$. We form a hermitian matrix S, the elements of which are

$$S_{ij} = \langle B_i B_j^* \rangle, \tag{A1}$$

where the asterisk denotes the complex conjugate and the angle brackets mean the average value over the frequency band used in analysis (see section 3). The matrix S is our estimate of the spectral matrix, apart from a factor of proportionality that depends on the duration of the snapshot and on the bandwidth of the analysis. In all calculations of the polarization parameters, this factor disappears; so we shall ignore it and refer to S loosely as the spectral matrix.

[41] In the next step, we apply the SVD algorithm to a real rectangular (6×3) matrix A, which is constructed from two square (3×3) matrices, one containing the real and the other the imaginary part of S. We use the SVD procedure [*Press et al.*, 1992] which decomposes A into the product of three matrices:

$$\mathsf{A} = \mathsf{U} \cdot \mathsf{W} \cdot \mathsf{V}^T, \tag{A2}$$

where U is a rectangular (6×3) matrix with orthonormal columns, W is a diagonal square (3×3) matrix containing three positive singular values w_i, and V is an orthonormal square (3×3) matrix.

[42] Now the columns of the matrix V define the directions of the axes of the polarization ellipsoid, and the corresponding singular values are related to the lengths of these axes. If the field is confined to a plane, one of the singular values is zero. For stationary random noise the singular values are proportional to the squares of the standard deviations of the field components in the respective directions. The planarity of the polarization can thus be defined as

$$F = 1 - \sqrt{w_1/w_3}, \tag{A3}$$

where w_1 is the smallest singular value and w_3 is the largest one. For $F = 0$ the three axes have the equal lengths, and the ellipsoid of polarization becomes a sphere; so there is no preferred direction for the field fluctuations. If $F = 1$, then the ellipsoid degenerates into an ellipse, and the directions of its axes are defined by the columns of V that correspond to the two nonzero singular values, w_2 and w_3. In this case, the ratio of the two axes of the polarization ellipse can be defined as

$$L_p = w_2/w_3. \tag{A4}$$

If $L_p = 0$, meaning that two of the singular values are zero, then the polarization is linear and the column of V corresponding to the remaining nonzero singular value (w_3) defines the direction of the fluctuations. If $0 < L_p < 1$, the polarization is elliptic, and if $L_p = 1$, the polarization is circular.

[43] Since L_p is positive, it is convenient, when graphing this quantity, to combine its value with the sense of the elliptic or circular polarization (that is, the sense of rotation of the magnetic vector around $\boldsymbol{B}_0$), as indicated by the sign of the imaginary part of the cross spectrum of the two perpendicular components. Thus we define the ellipticity of the polarization to be $L = L_s L_p$, where L_s is -1 when the polarization is left handed with respect to $\boldsymbol{B}_0$ (sense of the ion cyclotron motion), and L_s is $+1$ for right-handed polarization (sense of the electron cyclotron motion). For linear polarization, L_s is undefined, but both L and L_p are zero. In this paper, for comparison, we also use another definition of the ellipticity in terms of the elements in the first row of the spectral matrix [*Samson and Olson*, 1980].

[44] Another aspect of the field polarization is the mutual coherence of the field components, which is represented by the off-diagonal elements of S. Their values can lie in any quadrant of the complex plane, and averaging performed during the cross-spectral analysis may reduce their absolute values relative to the diagonal elements. This happens if the signal contains incoherent random phase shifts between the components. We use the SVD to define the plane of polarization in which we estimate a 2-D degree of coherence.

Since the columns of the matrix V give us the directions of the axes of the polarization ellipsoid, the matrix V^T transforms any vector to the coordinate system defined by these axes. The spectral matrix in that system is then

$$\mathsf{R} = \mathsf{V}^T \cdot \mathsf{S} \cdot \mathsf{V}. \tag{A5}$$

A 2-D degree of coherence in the plane of polarization can then be calculated from three of the nine elements of R,

$$C^2 = 2\left(R_{xx}^2 + R_{yy}^2 + 2|R_{xy}|^2\right)/(R_{xx} + R_{yy})^2 - 1, \tag{A6}$$

where the subscripts x and y denote the components corresponding to the two largest singular values (which are the lengths of the axes of the polarization ellipse in the case of plane polarization). C is 1 when the two components in the plane of polarization are perfectly coherent or when the polarization is linear. If the power carried by the two components is the same and if they have no mutual coherence ($R_{xy} = 0$), then C is zero. We also use a measure of 3-D coherence, the so-called degree of polarization defined by *Samson and Olson* [1980] as follows (the symbol tr denotes the trace of the matrix):

$$P^2 = \frac{3}{2}\,\mathrm{tr}\ \mathsf{S}^2/(\mathrm{tr}\ \mathsf{S})^2 - \frac{1}{2}. \tag{A7}$$

This quantity can be calculated without having to transform the spectral matrix, because it is invariant under changes of the coordinate system. Note that the equation for C is a 2-D version of the same formula.

[45] If the wave polarization is confined to the plane perpendicular to $\boldsymbol{B}_0$, the spectral matrix S has only four nonzero components. For a single elliptically polarized wave, these components are

$$\begin{aligned} S_{11} &= B^2\left[1 - \sin^2\phi\left(1 - L^2\right)\right] \\ S_{12} &= B^2\left[\cos\phi\sin\phi\left(1 - L^2\right) - iL\right] \\ S_{21} &= S_{12}^* \\ S_{22} &= B^2\left[1 - \cos^2\phi\left(1 - L^2\right)\right], \end{aligned} \tag{A8}$$

where the subscripts 1 and 2 denote the two components perpendicular to $\boldsymbol{B}_0$, B is the amplitude of the fluctuations, L is the ellipticity, and ϕ is the angle between the major polarization axis and axis 1, measured toward axis 2. Note that in the case of a single wave, the coherence is perfect, $C^2 = P^2 = 1$; it is imperfect only if we combine contributions from two or more waves with random phases as we do in the simulation in section 5.

[46] **Acknowledgments.** We thank J. Dowell and R. Brechwald, who wrote the preprocessing and calibration software for the HFWR and wideband data. This work was supported by NASA Goddard Space Flight Center under grant NAG5-7943. O. Santolík thanks the Fulbright commission in Prague for support during his stay in Iowa and acknowledges the support of Czech Grant Agency grant 205/01/1064.

References

Anderson, B. J., R. E. Denton, and S. A. Fuselier, On determining polarization characteristics of ion cyclotron wave magnetic field fluctuations, *J. Geophys. Res.*, *101*, 13,195–13,213, 1996.

André, M., Dispersion surfaces, *J. Plasma Phys.*, *33*, 1–19, 1985.

André, M., H. Koskinen, G. Gustafsson, and R. Lundin, Ion waves and upgoing ion beams observed by Viking, *Geophys. Res. Lett.*, *14*, 463–466, 1987.

Bergmann, R., Electrostatic ion (hydrogen) cyclotron and ion acoustic wave instabilities in regions of upward field-aligned current and upward ion beams, *J. Geophys. Res.*, *89*, 953–968, 1984.

Bergmann, R., and M. K. Hudson, Decay of electrostatic hydrogen cyclotron waves into ion acoustic modes on auroral field lines, *J. Geophys. Res.*, *92*, 2495–2504, 1987.

Cattell, C. A., F. S. Mozer, I. Roth, R. R. Anderson, R. C. Elphic, W. Lennartsson, and E. Ungstrup, ISEE 1 observations of electrostatic ion cyclotron waves in association with ion beams on auroral field lines from 2.5 to 4.5 R_E, *J. Geophys. Res.*, *96*, 11,421–11,439, 1991.

Cattell, C., et al., The association of electrostatic ion cyclotron waves, ion and electron beams and field-aligned current: FAST observations of an auroral zone crossing near midnight, *Geophys. Res. Lett.*, *25*, 2053–2056, 1998.

Chaston, C. C., et al., Characteristics of electromagnetic proton cyclotron waves along auroral field lines observed by FAST in regions of upward current, *Geophys. Res. Lett.*, *25*, 2057–2060, 1998.

Gurnett, D. A., et al., The Polar Plasma Wave Instrument, *Space Sci. Rev.*, *71*, 597–622, 1995.

Kintner, P. M., On the distinction between EIC waves and ion cyclotron harmonic waves, *Geophys. Res. Lett.*, *7*, 585–588, 1980.

Kintner, P. M., Plasma waves and transversely accelerated ions in the terrestrial ionosphere, *Phys. Fluids B*, *4*, 2264–2269, 1992.

Kintner, P. M., M. C. Kelley, and F. S. Mozer, Electrostatic hydrogen cyclotron waves near one Earth radius altitude in the polar magnetosphere, *Geophys. Res. Lett.*, *5*, 139–142, 1978.

Kintner, P. M., M. C. Kelley, R. D. Sharp, A. G. Ghielmetti, M. Temerin, C. Cattell, P. F. Mizera, and J. F. Fennell, Simultaneous observations of energetic (keV) upstreaming ions and electrostatic hydrogen cyclotron waves, *J. Geophys. Res.*, *84*, 7201–7212, 1979.

McFadden, J. P., C. W. Carlson, and R. E. Ergun, Microstructure of the auroral acceleration region as observed by FAST, *J. Geophys. Res.*, *104*, 14,453–14,480, 1999.

Mozer, F. S., R. Ergun, M. Temerin, C. Cattell, J. Dombeck, and J. Wygant, New features of time domain electric-field structures in the auroral acceleration region, *Phys. Rev. Lett.*, *79*, 1281–1284, 1997.

Press, W. H., P. B. Flannery, A. S. Teukolsky, and W. T. Vetterling, *Numerical Recipes*, Cambridge Univ. Press, New York, 1992.

Priestley, M. B., Spectral Analysis and Time Series, Academic, San Diego, Calif., 1989.

Rönnmark, K., Computation of the dielectric tensor of a Maxwellian plasma, *Plasma Phys.*, *25*, 699–701, 1983.

Roth, I., and M. K. Hudson, Lower hybrid heating of ionospheric ions due to ion ring distributions in the cusp, *J. Geophys. Res.*, *90*, 4191–4203, 1985.

Russell, C. T., and M. G. Kivelson, Detection of SO in Io's exosphere, *Science*, *287*, 1998–1999, 2000.

Samson, J. C., and J. V. Olson, Some comments on the descriptions of the polarization states of waves, *Geophys. J. R. Astron. Soc.*, *61*, 115–129, 1980.

Santolík, O., M. Parrot, and F. Lefeuvre, SVD methods for wave propagation analysis, *Radio Sci.*, doi:10.1029/2000RS002523, in press, 2002.

Stix, T. H., *Waves in Plasmas*, Am. Inst. of Phys., New York, 1992.

Temerin, M., and R. L. Lysak, Electromagnetic ion cyclotron mode (ELF) waves generated by auroral electron precipitation, *J. Geophys. Res.*, *89*, 2849–2859, 1984.

Yoshino, T., On the distribution of polar electrostatic emissions and their relationships to auroral hiss and direction finding measurements of saucer emission in polar regions observed by ISIS, Kyokko, and Akebono satellites, *Adv. Space Res.*, *11*(9), 45–50, 1991.

D. A. Gurnett and J. S. Pickett, Department of Physics and Astronomy, University of Iowa, Iowa City, IA 52242-1479, USA. (gurnett@space.physics.uiowa.edu; jsp@space.physics.uiowa.edu)

O. Santolík, Faculty of Mathematics and Physics, Charles University, V Holešovičkách 2, CZ-18000 Praha 8, Czech Republic. (ondrej.santolik@mff.cuni.cz)

L. R. O. Storey, Quartier Luchène, Route du Luberon, F-84160 Cucuron, France. (llewelyn.storey@physics.org)